JACS
JOURNAL OF THE AMERICAN CHEMICAL SOCIETY
pubs.acs.org/JACS
Article

Kinetics of Concurrent Seed Growth and Cation Exchange in Transforming $Cu_{2-x}S$ Nanocrystals to $CuGaS_2$ Nanorods

Yunpei Duan and Moonsub Shim*

Cite This: J. Am. Chem. Soc. 2025, 147, 9566−9575
Read Online
ACCESS | Metrics & More | Article Recommendations | Supporting Information

ABSTRACT: Cation exchange can convert nanocrystals that have already been achieved with a well-controlled size, size distribution, and shape to a broad range of compositions. However, cation exchange can often be accompanied by changes in the nanocrystal morphology/shape as exemplified by the synthesis of I−III−VI_2 nanocrystals. We examine the temperature-dependent kinetics of concurrently occurring seed epitaxial growth and cation exchange that convert nearly spherical $Cu_{2-x}S$ seeds into $CuGaS_2$ nanorods with varying lengths and degrees of tapering. A simple model is developed to quantify and explain experimentally observed reaction kinetics. Direct epitaxial growth of $Cu_{2-x}S$ seeds occurs with an activation energy of 96 kJ/mol, while cation exchange to convert the growing seed to $CuGaS_2$ requires overcoming a 202 kJ/mol energy barrier. Understanding how each reaction rate evolves over time provides insights into the tapering mechanism and a means of predicting when the onset of tapering occurs. The predicted onset is then exploited to synthesize nanorods with a minimized tapering. Our findings provide the basis for developing precise control over the composition and morphology of nanocrystals synthesized through a combination of cation exchange and solution epitaxy.

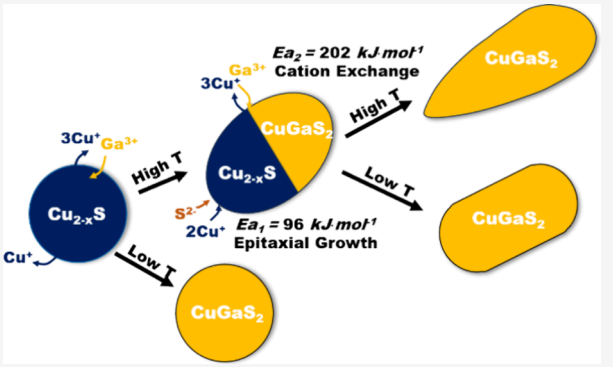

INTRODUCTION

Copper-based I−III−VI_2 ternary nanocrystals (NCs) and their derivatives offer significant potential for applications such as solar cells,[1] LEDs,[2] and imaging[3] without the environmental and biological toxicity that are inherent to currently prevalent Cd- and Pb-based counterparts.[4−7] These ternary NCs exhibit excellent light absorption coefficients (e.g., ~10^5−10^6 cm^{-1} for $CuInS_2$[8,9] and $CuGaS_2$[9]) and tunable band gaps.[10] They can also accommodate a wide range of cation-to-cation and cation-to-anion ratios without a drastic change in the crystal structure, affording an additional parameter through which their properties can be tuned.[11,12] However, the growth mechanisms of these NCs are often complex and therefore, the synthetic control over their size and size distribution has been more difficult to achieve.[13,14] This complexity has also led to a variety of interesting shapes but usually as serendipitous results rather than the intended outcomes. Compared to the synthesis of more established II−VI colloidal quantum dots, direct synthesis of I−III−VI_2 NCs requires a careful balance of the different reactivities of multiple cation and anion precursors,[13,15] and their nucleation and growth can often deviate from the well-known LaMer model.[16] Therefore, the size uniformity and chemical homogeneity of the final products from direct synthesis are often inferior to those of II−VI semiconductors. Alternatively, cation exchange offers a versatile route that can lead to improved size and shape uniformity, as well as to a variety of morphologies, compositions, crystal structures, and complexity (e.g., core/shell heterostructures,[17] alloys,[18,19] and Janus particles[20]).

$Cu_{2-x}S$ (typically x = 0−0.3)[21] is commonly employed as the parent or the intermediate material for cation exchange.[22−25] Among I−III−VI_2 materials, $CuInS_2$ and $CuGaS_2$ have been studied the most with respect to cation exchange involving $Cu_{2-x}S$ seeds.[19,20,26−28] According to the hard−soft acid−base (HSAB) theory, In^{3+} and Ga^{3+} are hard Lewis acids, whereas Cu^+ is relatively soft.[29] As a result, softer Lewis bases such as thiols and TOP exhibit a stronger affinity toward Cu^+, facilitating the cation exchange process. Furthermore, $Cu_{2-x}S$ typically contains a high density of Cu^+ vacancies and exhibits high Cu^+ diffusivity,[28,30] providing a favorable condition for the cation exchange. There have been several studies examining kinetics and mechanisms of cation exchange using $Cu_{2-x}S$ NCs as templates.[18,24,28,31] Thiel et al. reported a vacancy-assisted mechanism of In^{3+} exchange on $Cu_{2-x}S$ nanorods with activation energy varying around the phase transition temperature, below which the exchange is

Received: December 9, 2024
Revised: February 20, 2025
Accepted: February 21, 2025
Published: March 4, 2025

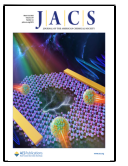

limited to the surface.[28] Le et al. increased the cation exchange yield by oxidizing $Cu_{2-x}S$ with I_2, creating more Cu vacancies to facilitate the exchange.[31] However, many cation exchange reactions have also often led to uncontrolled simultaneous changes in the morphology, which suggests another process to be concurrently occurring.[18,20,32−34] For instance, In^{3+} exchange using $InCl_3$ on $Cu_{2-x}S$ nanoplatelets results in hollow structures.[34] Whether introduced as seed particles or grown *in situ*, $Cu_{2-x}S$ NCs can evolve into rod-shaped heterostructures with $CuInS_2$, $CuGaS_2$, ZnS, CoS, or CdS, which can eventually be converted completely to single-phase I−III−VI_2, II−VI, or other sulfide nanorods.[20,24,27] Many factors, such as temperature, time, concentration, and precursor and ligand chemistry, affect growth mechanisms and kinetics, making them difficult to understand. Therefore, despite a variety of compositions and morphologies having been reported, synthetic control over these fundamental parameters through rational means remains elusive.

Here, we report on the growth mechanism and kinetics of the evolution of "spherical" $Cu_{2-x}S$ seed NCs to $CuGaS_2$ nanorods with varying lengths of tapering. We investigate the kinetics in the reaction temperature range of 160 to 240 °C, considering the Concurrent Seed growth and Cation exchange (CSC) mechanism.[32] In the CSC, epitaxial growth of $Cu_{2-x}S$ occurs directly at one end of the $Cu_{2-x}S$ seed, while cation exchange from $Cu_{2-x}S$ to $CuGaS_2$ occurs at the interface between the two phases. The latter reaction requires an initial nucleation of $CuGaS_2$ within the $Cu_{2-x}S$ phase before growth through continued conversion of $Cu_{2-x}S$ to $CuGaS_2$ can occur. We show that a partial loss of Cu^+ ions from the seed $Cu_{2-x}S$ NCs occurs first, leading to Cu^+ in solution necessary for the epitaxial growth of $Cu_{2-x}S$ to initiate as well as Cu-deficient seed NCs that facilitate cation exchange. The rates of seed epitaxial growth and cation exchange are dictated by the different activation energies of each reaction, the difference in the temperature dependence of their respective rate constants, and the time-varying solution concentrations of Cu^+ ions that are generated through cation exchange and consumed by epitaxial growth. The varying rates of the two reactions over the course of growth are manifested in the different final volumes and the degree of tapering of the resulting $CuGaS_2$ nanorods at different temperatures, indicating that these features can be controlled simply by the reaction temperature.

RESULTS AND DISCUSSION

Nanoparticles of $CuGaS_2$ have been reported in several different morphologies,[18,35−37] and many, if not most, involve cation exchange of $Cu_{2-x}S$ NCs that are often generated *in situ*. In the one-pot heat-up synthesis of $CuGaS_2$ nanorods, $Cu_{2-x}S$ NCs have been shown to appear at the beginning of the reaction.[32] The subsequent elongation into nanorods has been attributed to solution epitaxial growth of the seed $Cu_{2-x}S$ NCs while a cation exchange reaction concurrently converts the growing seeds into tapering $CuGaS_2$ nanorods. Although the single-pot approach makes synthesis simpler, different reaction steps that can occur simultaneously makes it difficult to examine the growth kinetics. In order to separate the seed epitaxial growth and cation exchange from potential complications of the initial $Cu_{2-x}S$ nucleation, we first synthesized $Cu_{2-x}S$ NCs separately, purified them, and then injected them as seeds into the reaction mixture that contained Ga and S precursors. 1-Dodecanethiol (1-DDT) was used as the ligand, sulfur source, and solvent. To simplify the kinetics of the cation exchange process as much as possible, no additional solvent or ligands were introduced. Aliquots were taken throughout the reaction for characterization. The size distribution of the final $CuGaS_2$ nanorods obtained from the two-pot method examined here appears to be more uniform, presumably due to starting with more uniform $Cu_{2-x}S$ seeds. The analysis of the lattice fringes of the $Cu_{2-x}S/CuGaS_2$ Janus particle from HRTEM (Figure S1) shows the same heterointerfaces as the intermediates of the single-pot synthesis. The 138° angle between the $Cu_{2-x}S/CuGaS_2$ interface and (0001) plane closely matches the expected angle between $(10\bar{1}2)$ and (0001) for wurtzite $CuGaS_2$ and the low-chalcocite phase of $Cu_{2-x}S$. The crystallographic indices used here refer to the hexagonal S sublattice for simplicity. The only significant difference between the single-pot and two-pot approaches appears to be the average length of the final $CuGaS_2$ nanorods, which is shorter for the latter approach and depends on the reaction temperature.

Initial Cu^+ Loss from Seed Nanocrystals. Transmission electron microscopy (TEM) images of the seed $Cu_{2-x}S$ NCs and aliquots taken at different times after seed injection for the reaction at 200 °C are shown in Figure 1a−d. Powder X-ray

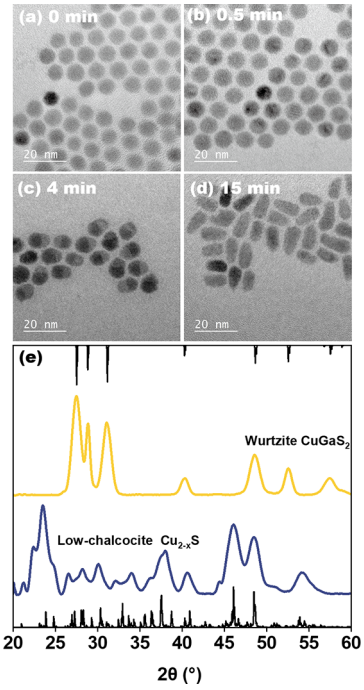

Figure 1. CSC growth at 200 °C. (a−d) TEM images of particles at different stages: (a) 7 nm $Cu_{2-x}S$ seeds NCs, (b) 0.5 min after seed injection, showing some contrast difference, (c) 4 min after seed injection, $Cu_{2-x}S/CuGaS_2$ Janus particles, and (d) after 15 min, $CuGaS_2$ nanorods. (e) Powder XRD patterns of $Cu_{2-x}S$ seeds (yellow) and final $CuGaS_2$ nanorods (blue), with the reference pattern of low-chalcocite $Cu_{2-x}S$ (bottom, ICDD-PDF No. 04-026-0650) and wurtzite $CuGaS_2$ (top, simulated).

diffraction of the starting $Cu_{2-x}S$ seeds and the final $CuGaS_2$ nanorods indicates that the initial low-chalcocite structure converts to wurtzite $CuGaS_2$ (Figure 1e). There appears to be a slight decrease in the average particle diameter from initial $Cu_{2-x}S$ seeds to 30 s after injection, followed by the formation of $Cu_{2-x}S/CuGaS_2$ Janus particles as seen in the 4 min image and eventual growth and conversion to single-phase $CuGaS_2$

https://doi.org/10.1021/jacs.4c17582
J. Am. Chem. Soc. 2025, 147, 9566−9575

nanorods. Despite adding purified $Cu_{2-x}S$ NC seeds without any additional Cu^+ reagents, the growth stages are quite similar to the single-pot synthesis previously reported.[32] The volume of the NCs can expand more than three times the initial $Cu_{2-x}S$ seeds even without any additional Cu^+ reagent being added. This observation begs the following question: where do the Cu^+ ions that need to be incorporated into the final $CuGaS_2$ nanorods come from?

The histograms of diameter measured from TEM images of the seed $Cu_{2-x}S$ NCs and aliquots collected from 10 to 30 s show that the size of particles decreases from 7.1 ± 0.6 nm seeds to 6.1 ± 0.7 nm at 20 s after injection at 200 °C (Figure 2a). The size begins to increase afterward. Figure 2b shows the

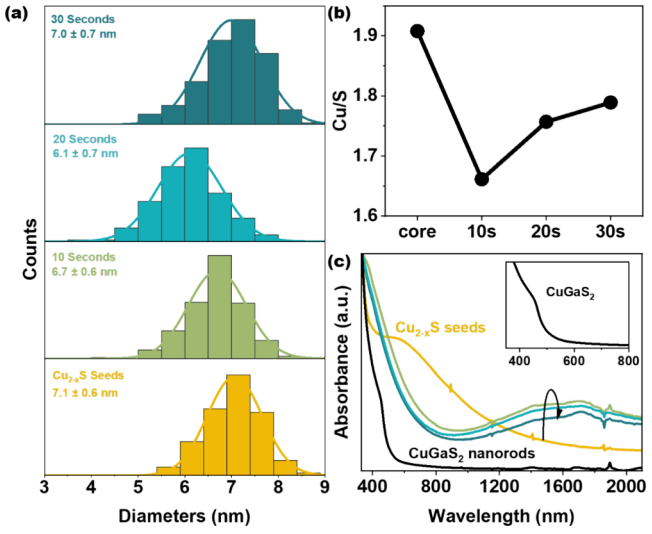

Figure 2. Initial Cu^+ loss from seed NCs at 200 °C. (a) Diameter histograms of particles at indicated reaction times, (b) Cu/S ratio measured from large-area STEM-EDX elemental analysis, and (c) Vis-NIR spectra of $Cu_{2-x}S$ seeds (yellow), at early reaction stages (starting from green to decreasing absorption in the NIR: 10, 20, and 30 s respectively), and final $CuGaS_2$ nanorods (black).

Cu/S ratio measured from large-area EDX scans for the early stages of the growth. Examples of TEM images, dark-field STEM images, and corresponding EDX spectra are shown in Figure S2. During the first ∼20 s of the reaction, the Cu/S ratio decreases from ∼1.9 to below 1.7, with Ga detected at less than 0.5% (Table S1). TEM images, as shown in Figure 1, indicate that noticeable $CuGaS_2$ domains do not appear until after ∼30 s, and therefore, the EDX results may be interpreted as $Cu_{2-x}S$ NCs becoming Cu-deficient at early stages of the reaction. Vis-NIR absorption spectra in Figure 2c further confirm that the seed NCs first become Cu-deficient at the beginning of the reaction. Nearly stoichiometric $Cu_{2-x}S$ seeds exhibit only an absorption shoulder in the visible that tails out weakly into the NIR. At 10 s after the seed injection, a strong localized surface plasmon resonance (LSPR) appears in the NIR, consistent with Cu-deficient $Cu_{2-x}S$ NCs.[38] The intensity of the LSPR decreases over time, which is consistent with the Cu/S ratio measured by EDX in Figure 2b. By 30 s, the particles start to exhibit some contrast difference, indicating the initial formation of $CuGaS_2$ (Figure 1b). After 15 min, the LSPR signal is lost and the appearance of an absorption shoulder at ∼455 nm (2.72 eV), which is slightly higher in energy than the reported band gap of bulk wurtzite structure $CuGaS_2$ (2.53 eV),[39] indicates full conversion to $CuGaS_2$.

These results together reveal that there is a loss of Cu^+ from the initial seed NCs, which becomes the feedstock for growth of $Cu_{2-x}S$ via solution epitaxy. This loss also facilitates cation exchange, which requires the removal of Cu^+ ions from the seed NCs. If all Cu^+ used to form the $CuGaS_2$ nanorods came only from the $Cu_{2-x}S$ seed NCs and considering that the equivalent anion sublattice unit of $CuGaS_2$ should be about 18% smaller in volume than that of $Cu_{2-x}S$, then a factor of 3.3 increase in volume can be expected. As shown below, the average volume of the final $CuGaS_2$ nanorods grown at the highest reaction temperature examined here, which leads to the longest nanorods, is 654 ± 119 nm^3. Compared to the initial seed $Cu_{2-x}S$ volume of 186 ± 42 nm^3, this final volume corresponds to a factor of 3.5 increase, close to the factor of 3.3 in the ideal limit of using Cu^+ only from the seed NCs. Then, we conclude that the Cu^+ source for the growth of $CuGaS_2$ nanorods is essentially all from the initial $Cu_{2-x}S$ NCs and that the initial loss of Cu^+ from the seeds is a necessary first step for both solution epitaxial growth of the seeds and the concurrent cation exchange reaction to convert the growing $Cu_{2-x}S$ NCs into $CuGaS_2$. Note that in the one-pot synthesis[32] where $Cu_{2-x}S$ NCs are generated *in situ*, there is an excess amount of Cu^+ in the reaction mixture and therefore the final $CuGaS_2$ nanorods can be much longer.

Temperature Dependence of $CuGaS_2$ Nanorod Growth. In order to gain insights on the growth kinetics beyond the initial Cu^+ loss, we now consider how the evolution of $Cu_{2-x}S$ seeds to $CuGaS_2$ nanorods occurs at different reaction temperatures (from 160 to 240 °C). The overall reaction rate varies considerably with temperature, as indicated by the length of time for the reaction mixture to turn light yellow. This color change occurs within 150 s when the seed injection and growth are carried out at 240 °C, while it takes around 6 h at 160 °C. TEM images of the $Cu_{2-x}S$ seeds and the final products obtained at different reaction temperatures are shown in Figure 3a–f. There is a monotonic increase in the length of the $CuGaS_2$ nanorods with increasing temperature with very little change in the diameter of the "head" region (Figure 3g). All cases shown here start from the same batch of $Cu_{2-x}S$ seeds, which exhibit a nearly spherical shape (Figure 3a). Elemental maps of these seed NCs obtained from EDX show a uniform distribution of Cu and S throughout the NCs (Figure S3). The product from reaction at 160 °C remains nearly spherical with slight irregularities in shape, but the composition has changed to $CuGaS_2$, as shown by the EDX elemental maps (Figure S4). The slow conversion of $Cu_{2-x}S$ to $CuGaS_2$ without a significant change in the overall size and shape indicates that cation exchange is the dominant reaction at this temperature. The dominance of cation exchange is due to the temperature at which active S species is generated. Control experiments where Cu and S precursors are heated up to 160 or 180 °C at a rate of about 30 °C/min (Figure S5) show that no $Cu_{2-x}S$ NCs are formed at 160 °C even after overnight. At 180 °C, the reaction mixture begins to change color at about 10 s after reaching the reaction temperature and turns dark brown within 1 min (much faster than the completion of CSC reaction at 180 °C of ∼40 min), indicating formation of $Cu_{2-x}S$ NCs. These results suggest that there is a relatively narrow temperature range at which 1-DDT converts to active S species between 160 and 180 °C.

Assuming the S sublattice to be the anion sublattice structure of wurtzite crystals for both the seed $Cu_{2-x}S$ and the final $CuGaS_2$, the equivalent unit cell volumes are 91.6 $Å^3$

https://doi.org/10.1021/jacs.4c17582
J. Am. Chem. Soc. 2025, 147, 9566−9575

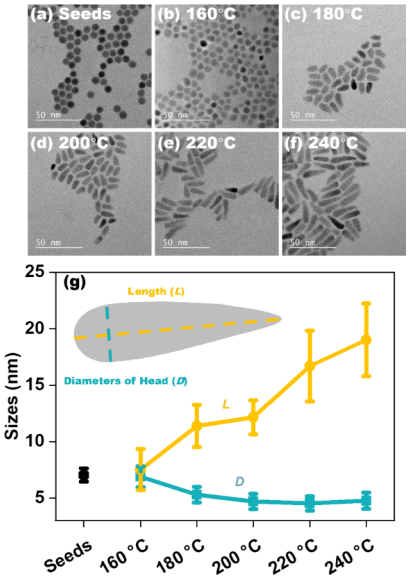

Figure 3. Temperature dependence of $CuGaS_2$ nanorod growth. (a) TEM image of $Cu_{2-x}S$ seeds NCs. TEM images of $CuGaS_2$ nanorod products grown at (b) 160 °C, (c) 180 °C, (d) 200 °C, (e) 220 °C, and (f) 240 °C. (g) Length (L, filled yellow circles) and diameters of head (D, filled green squares) of final $CuGaS_2$ nanorods grown at the indicated reaction temperatures. The inset shows a schematic of $CuGaS_2$ nanorod dimensions.

(two Cu_2S unit equivalent, $v_{c,o}$)[40] and 75.0 Å^3 (one $CuGaS_2$ unit equivalent, $v_{g,o}$), respectively. This means that the complete cation exchange from $Cu_{2-x}S$ to $CuGaS_2$ without any additional growth should lead to about an 18% decrease in volume. The fact that the average diameter, and therefore the average volume, does not change significantly for reaction at 160 °C may mean that there is a small but non-negligible amount of growth. For a starting $Cu_{2-x}S$ seed volume of 186 nm^3, maintaining this volume while completely converting to $CuGaS_2$ corresponds to about 450 $CuGaS_2$ units added or about 22% increase in the number of S sublattice unit cells per NC. Then, the relatively small change in the average size can be attributed to the reaction temperature being near or just below the thermolysis temperature of 1-DDT, the S source—i.e., there is only a small amount of reactive S available for the addition of cations and anions together to the seed NCs. We note that the product of the 160 °C reaction (Figure 3b) exhibits many particles that are slightly distorted with a possible hint of tapering as well as particles that are noticeably smaller than the starting $Cu_{2-x}S$ seed NCs. Such a distribution in size/shape is consistent with some particles (larger slightly distorted particles) undergoing a small degree of growth and cation exchange via CSC mechanism and another subset of particles (the smaller particles) undergoing only cation exchange. We note that the smaller particles may also arise from a combination of cation exchange and slight etching (e.g., surface Cu^+ loss may be accompanied by surface S^{2-} loss), which we cannot yet verify.

At higher reaction temperatures, the final $CuGaS_2$ products have a rod-like morphology with length and tapering that depend on the temperature (Figure 3c–f). The average length increases from 7.5 nm at 180 °C to 19.0 nm at 240 °C (Figure 3g). For this temperature range, the average "head" diameter

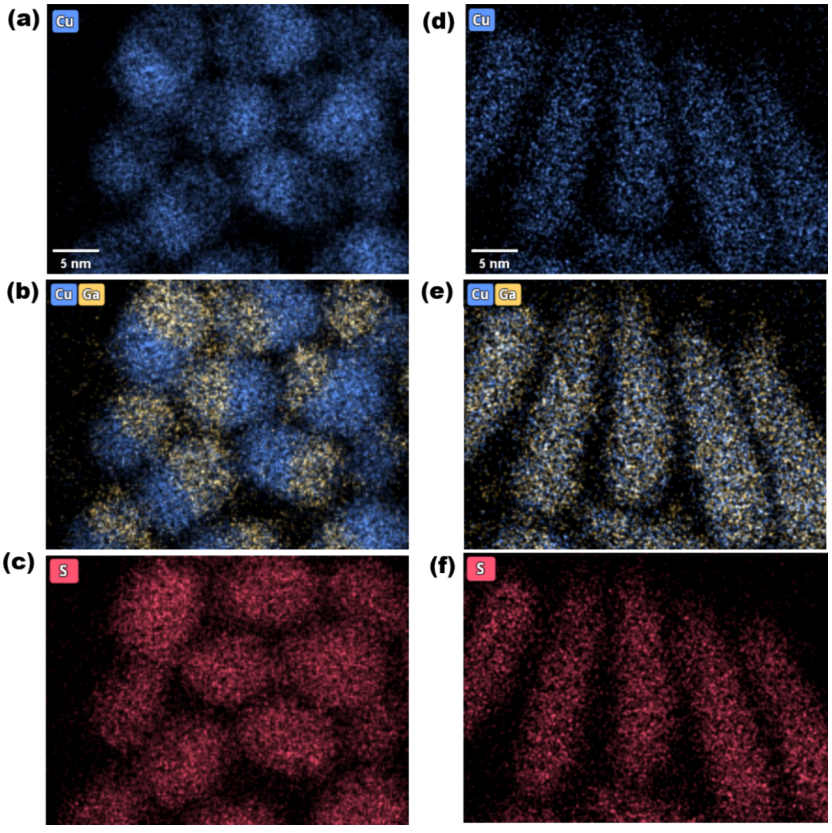

Figure 4. EDX elemental maps of (a–c) Janus particles grown for 2 min and (d–f) nanorods grown for 7 min at 220 °C. (a) and (d) are Cu, (b) and (e) are Cu and Ga composite, and (c) and (f) are S maps.

https://doi.org/10.1021/jacs.4c17582
J. Am. Chem. Soc. 2025, 147, 9566–9575

decreases to ∼5 nm, from the initial $Cu_{2-x}S$ seed diameter of 7.1 nm. In addition, increasing reaction temperature causes more pronounced tapering—i.e., longer length where tapering is occurring. As noted earlier, the length increase for the reaction carried out at 240 °C agrees closely with the expected volume increase if all Cu^+ ions exchanged out from the seed $Cu_{2-x}S$ NCs were reincorporated into the final product as $CuGaS_2$. For all temperatures, the composition of the final product is $CuGaS_2$ but the average length and, therefore, the average volume increase with temperature. Then, the smaller final volume at lower reaction temperatures means that some of the Cu^+ ions exchanged out from the seed NCs remain in the solution. The "head" diameter of the final $CuGaS_2$ nanorods being smaller than the seed $Cu_{2-x}S$ NC diameter may be expected based on a smaller S sublattice unit cell volume for $CuGaS_2$, but there may also be partial etching of the $Cu_{2-x}S$ seeds at the beginning of the reaction, as mentioned earlier.

Figure 4 shows the EDX elemental maps from aliquots taken at two different time points of the reaction carried out at 220 °C. At 2 min, Cu is present in all parts of each ellipsoidal NC but is more concentrated in one-half (Figure 4a). Ga is present only in half of each NC where there is less Cu (Figure 4b), whereas S is uniformly present (Figure 4c). Continued reaction leads to the elongation of the $CuGaS_2$ segment with a decreasing size of the $Cu_{2-x}S$ tip. At the end of the reaction (7 min), all three elements, Cu, Ga, and S, are uniformly distributed in the tapering nanorods (Figure 4d–f). Cu and Ga composition ratios obtained from large-area EDX measurements over the course of the reaction for all temperatures examined here reveal a decreasing Cu/Ga ratio over time, ending with a value of ∼1 expected for $CuGaS_2$ (Figure S6). These observations are consistent with the CSC growth mechanism where $Cu_{2-x}S/CuGaS_2$ Janus particles form via cation exchange and the elongation of the nanorods occurs via epitaxial growth of the $Cu_{2-x}S$ tip, which is converted to $CuGaS_2$ due to continued cation exchange.

Kinetic Model of CSC Growth. The temperature dependence of length and tapering and the initial Cu^+ loss from the seed $Cu_{2-x}S$ NCs described above are all in qualitative agreement with the CSC growth mechanism. That is, the competition between solution epitaxial growth of $Cu_{2-x}S$ and cation exchange that converts $Cu_{2-x}S$ to $CuGaS_2$ can lead to tapering nanorods. We now consider a simple kinetic model to describe each of these two competing reactions more quantitatively and compare to experimental results. Note that solution epitaxial growth does not occur directly in the $CuGaS_2$ phase. Hence, we impose the condition that $CuGaS_2$ can grow only via cation exchange. Then, the seed growth and cation exchange reactions can be described by the following chemical equations:

$$2Cu^+ + S^{2-} \xrightarrow{k_1} (Cu_{2-x}S)_{NC} \quad (1)$$

$$2(Cu_{2-x}S)_{NC} + Ga^{3+} \xrightarrow{k_2} (CuGaS_2)_{NC} + 3Cu^+ \quad (2)$$

where k_1 is the rate constant for the epitaxial growth of $Cu_{2-x}S$, and k_2 is the rate constant for cation exchange of Cu^+ for Ga^{3+}. According to hard–soft acid–base theory, thiols are relatively soft Lewis bases ($\eta \sim 4$–6 eV) and Cu^+ is a relatively soft acid ($\eta = 6.28$ eV),[29] but Ga^{3+} is a hard acid ($\eta \sim 17$ eV).[41] While both Cu^+ and Ga^{3+} can form complexes with 1-DDT, Cu^+ should have a much stronger affinity to thiols/thiolates. This difference in affinity makes cation exchange thermodynamically favorable and should drive the Cu^+ loss from the seed $Cu_{2-x}S$ NCs. 1-DDT is present in excess as ligand, S source, and solvent, and therefore, its concentration can be assumed to be constant throughout the reaction. Reaction 1 is a surface reaction where Cu^+ and S^{2-} ions add to the existing $Cu_{2-x}S$ NCs and assumed to be first order with respect to $[Cu^+]$ in solution.[42] Cation exchange takes place at the heterointerface between $Cu_{2-x}S$ and $CuGaS_2$ phases and is assumed to be first order with respect to $[Ga^{3+}]$ in solution. These considerations lead to the following rate equations:

$$-\frac{d[Cu^+]}{dt} = k_1[Cu^+] - 3k_2[Ga^{3+}] \quad (3)$$

$$-\frac{d[Ga^{3+}]}{dt} = k_2[Ga^{3+}] \quad (4)$$

With the initial concentrations $[Ga^{3+}]_0$ and $[Cu^+]_0$ in solution, the corresponding integrated rate equations are

$$[Cu^+] = ([Cu^+]_0 - 3\frac{k_2[Ga^{3+}]_0}{k_1 - k_2})e^{-k_1 t} + 3\frac{k_2[Ga^{3+}]_0}{k_1 - k_2}e^{-k_2 t} \quad (5)$$

$$[Ga^{3+}] = [Ga^{3+}]_0 e^{-k_2 t} \quad (6)$$

Note that $[Ga^{3+}]_0$ is an effective initial concentration since the amount of Ga^{3+} that can be incorporated into the NC via cation exchange is limited by the number of cation sites in the crystal (or the number of Cu^+ ions that are removed from the lattice). Especially at low reaction temperatures, this can also be limited by the amount of reactive S^{2-} available. The initial concentration of Cu^+ in solution, $[Cu^+]_0$, for reactions 1 and 2 should be determined by the early-stage Cu^+ loss.

In order to relate the concentrations to experimentally measured quantities, we consider the average volume of growing NCs. From the time series of TEM images of aliquots taken during each reaction, the average volume change of both the total particle and $CuGaS_2$ phase can be estimated. When a particle's shape is known, calculating the volume from a 2D TEM image is straightforward. However, in our case, most stages of the reaction yield irregular rod-like shapes. Hence, the vertical rotator principle exploiting the Pappus–Guldinus theorem has been used here to estimate the volume of each NC by rotating each planar TEM image about an axis in the plane.[43] Figure S7 illustrates how the total volume of an NC is estimated from a planar image using this principle. The volume of the $CuGaS_2$ portion in each particle can also be estimated in this manner but is significantly more difficult as each $CuGaS_2$ region needs to be carefully defined. Hence, the ratio of Cu/Ga measured by large-area STEM-EDX was used to estimate the $CuGaS_2$ volume, assuming stoichiometries of Cu_2S and $CuGaS_2$ and $v_{c,o}$ and $v_{g,o}$ values given earlier. Estimated volumes of multiple particles measured for each reaction condition are averaged to give V_g and V, the average volume of the $CuGaS_2$ phase per NC and the average total particle volume, respectively. Taking into account that there are 4 Cu^+ ions per $v_{c,o}$ and only one Ga^{3+} per $v_{g,o}$, the relations between the change in the total and $CuGaS_2$ volumes per NC and the number of cations lost from the solution are then given by

$$dV = -\frac{v_{c,0}}{4}dn_c \quad (7)$$

https://doi.org/10.1021/jacs.4c17582
J. Am. Chem. Soc. 2025, 147, 9566–9575

$$dV_g = -v_{g,0}dn_g \tag{8}$$

n_c and n_g are the number of Cu^+ and Ga^{3+} ions in solution, respectively, and are normalized with respect to the number of particles in solution, which is assumed to be constant. The integrated rate equations can now be written in terms of per particle volumes, V and V_g. However, reaction 2 does not account for the nucleation step needed for the initial formation of the $CuGaS_2$ phase. The well-established Kolmogorov, Johnson, Mehl, and Avrami (KJMA) theory can be used to describe the relationship between nucleation rate, growth rate, and time through the Avrami exponent.[44,45] Epitaxial growth of $Cu_{2-x}S$ in reaction 1 does not require a separate nucleation step, since it is homoepitaxy. Hence, the exponent n is introduced only for the cation exchange reaction 2, and the integrated rate equations can be rewritten as

$$V = V_0 - \frac{v_{c,0}}{4}\left[c_0\left(e^{-k_1 t} - 1\right) - 3\frac{k_2 g_0}{(k_1 - k_2)}\left(e^{-k_2 t^n} - e^{-k_1 t}\right)\right] - \frac{v_{c,0} - v_{g,0}}{2}g_0\left(1 - e^{-k_2 t^n}\right) \tag{9}$$

$$V_g = v_{g,0}g_0\left(1 - e^{-k_2 t^n}\right) \tag{10}$$

Again, $v_{c,o}$ and $v_{g,o}$ are the volumes of the $(Cu_{2-x}S)_2$ and $CuGaS_2$ units, respectively. c_0 is the initial number of Cu^+ ions in solution, normalized to the number of NCs in solution (which remains constant), since the volumes are per NC values. Again, similar to $[Ga^{3+}]_0$, g_0 is the effective number of Ga^{3+} ions per NCs, which is limited by available cation sites in the NC or reactive S^{2-}. Therefore, g_0 is the total number of Ga^{3+} ions that can be incorporated into each nanorod. Note that at the end of the reaction, the final nanorod volume is equal to the product of $v_{g,o}$ and g_0. V_0 is the initial particle volume (i.e., is the average volume of the $Cu_{2-x}S$ seeds). In the ideal limit, there should be no Cu^+ present in the solution at $t = 0$ (i.e., $c_0 = 0$). However, as discussed previously, there is an initial loss of Cu^+ from the seed particles and with the reaction time being significantly longer than this period of initial Cu^+ loss, we set $c_0 \neq 0$ and use it as a fitting parameter. The last term in eq 9 accounts for the effect of the difference in the sublattice volumes of $Cu_{2-x}S$ and $CuGaS_2$. However, this contribution is negligible compared to the initial decrease in volume and the uncertainty in measured volume arising from finite size distribution. Therefore, we do not include this term in our fitting. Note that removing this term still leads to same functional form for the time dependence and will lead to the same fitting values for the rate constants.

Integrated rate eqs 9 and 10 were used for least-squares fitting of measured volumes, V and V_g, with k_1, k_2, c_0, g_0, and n as fitting parameters (Figure 5a,b). Note that these results are plotted to time normalized to completion time (degree of completion) such that reactions with different temperatures can be compared (cf. completion times for 240 and 160 °C reactions are 5 min and 6 h, respectively). As mentioned earlier, the average volume does not change significantly from the initial seed $Cu_{2-x}S$ NCs at 160 °C, indicating that cation exchange is dominant without much epitaxial growth. Thus, only the cation exchange results are fitted at this temperature. The temperature dependence of k_1 and k_2 obtained from the fitting is shown in Figure 5c and Figure 5d. Both rate constants exhibit Arrhenius behavior with activation energies of Ea_1 = 96 kJ/mol for solution epitaxy and Ea_2 = 202 kJ/mol for cation exchange. This value for Ea_2 is in the range of $\sim 10^2$ kJ/mol reported for vacancy-mediated cation exchange.[46]

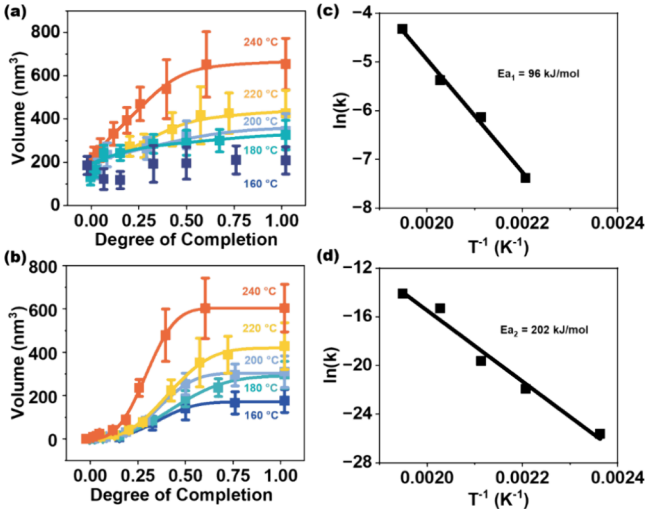

Figure 5. (a) Evolution of average total volumes of particles over time at indicated temperatures with kinetic model fits using eq 9 (solid lines). Degree of completion corresponds to reaction time normalized to final time to allow comparison across different temperatures. (b) Same for the $CuGaS_2$ portion of the volume but using eq 10 for kinetic model fits. (c) Arrhenius plot of epitaxial growth rate constant k_1 along with linear fit. (d) Arrhenius plot of cation exchange rate constant k_2 along with linear fit.

These fitting results also provide insights into the temperature dependence of c_0 and g_0, and the Avrami exponent. Both c_0 and g_0 exhibit Arrhenius behavior (Figure S8). Thermal activation behavior of c_0, the initial Cu^+ concentration, is consistent with our assumption that Cu^+ diffusion out of the seed $Cu_{2-x}S$ particles establishes c_0. The same type of behavior for g_0 can also be expected since it is dependent on the volume of the final particles, which increases with temperature through reactions with rate constants that exhibit Arrhenius behavior (Figure 5). The values of n obtained from the curve fitting are around 3 across all temperatures (Figure S9), indicating that the cation exchange follows the same mechanism at the range of temperatures that we explored. Note that a more proper way to obtain the Avrami constant would be to consider the fraction of the total volume converted by cation exchange. However, in our case, the total volume changes with time. In fact, both V_g and V change with time, as shown in Figure 5a,b. Including this effect and fitting the experimental values of V_g/V to $1 - e^{-k_2 n*}$ lead to Avrami exponent, $n*$, being close to 2, which can be interpreted as a nucleation process and diffusion-controlled, two-dimensional growth (Figure S10).[44]

Despite the larger activation energy, cation exchange can be significant or even dominate in the reaction temperature range explored here. As discussed earlier, at 160 °C or below, very little to no thermal decomposition of thiols needed to generate the active S species occurs, and therefore cation exchange dominates. At higher reaction temperatures, effective cation concentrations along with the rate constants will determine the actual reaction rates. Figure 6a,b shows the reaction rates, plotted as the change in volume over time (dV/dt) from the fitting results of Figure 6a,b, for the homoepitaxial growth (dashed lines) and cation exchange (solid lines) at different temperatures. All reaction temperatures studied exhibit a

https://doi.org/10.1021/jacs.4c17582
J. Am. Chem. Soc. 2025, 147, 9566−9575

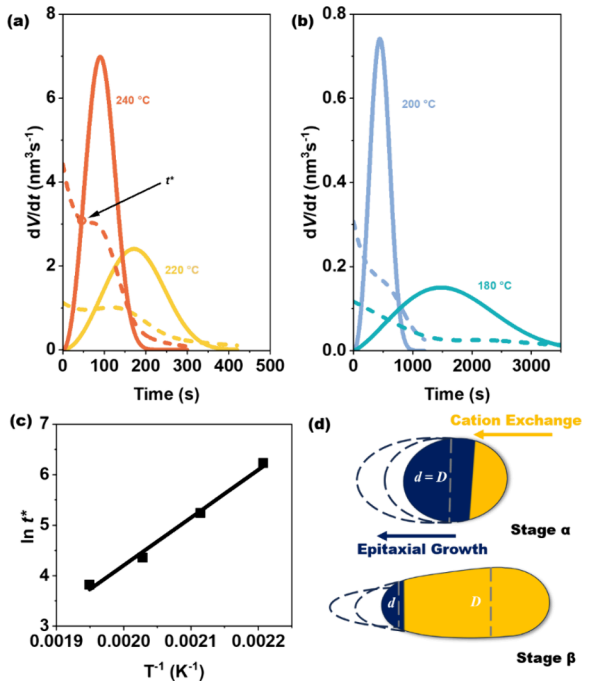

Figure 6. (a) Epitaxial rate and cation exchange rate at 240 and 220 °C. The arrow points to the time (t^*) at which the epitaxial and cation exchange rates are equal, shown only for reaction at 240 °C as an example. (b) Same for reactions at 200 and 180 °C. (c) Plot of ln(t^*) versus inverse temperatures along with a linear fit. (d) Schematics of two growth stages. At stage α, the active diameter at the interface, d, is equal to the diameter of the head, D. At stage β, d is smaller than D and continues to decrease, leading to tapering.

similar pattern. In the early stages, epitaxial growth proceeds efficiently, as it does not require a nucleation process. In contrast, growth via cation exchange must first undergo a heterogeneous nucleation process, resulting in a lower initial reaction rate despite the ample presence of Ga^{3+} in the solution. As Cu^+ in the solution is consumed, the rate of epitaxial growth decreases. Meanwhile, cation exchange accelerates and exceeds the epitaxial growth. The Cu^+ produced by cation exchange compensates for the consumed Cu^+ in the solution, slowing the decrease in the epitaxial growth rate or even reversing it into acceleration. After this point, both processes begin to decelerate until the reaction is completed. In principle, the two processes should cease simultaneously and the slight nonzero tails of epitaxial rates are within the error of our fitting.

The point at which the cation exchange rate overtakes the epitaxial growth rate (t^*) is when the rate of volume change of the $Cu_{2-x}S$ portion goes through zero—i.e., the $Cu_{2-x}S$ tip starts to decrease in size. This decrease then causes the subsequent cation exchange to produce progressively smaller diameter $CuGaS_2$, leading to observed tapering. Similar to the rate constants, the temperature dependence of t^* also follows the Arrhenius behavior (Figure 6c). The schematics in Figure 6d depict the two stages before and after this critical time point. Stage α corresponds to growth without tapering, while stage β represents the growth after t^*, i.e., tapering growth.

As an example application of this insight into designing NC morphology, we have carried out a reaction at 220 °C but quickly quenched the reaction temperature to 160 °C prior to t^*. This temperature quench should minimize epitaxial growth of $Cu_{2-x}S$ but still allow cation exchange to continue, thereby eliminating tapering. Figure 7 compares two cases where the first reaction was allowed to complete at a fixed temperature of

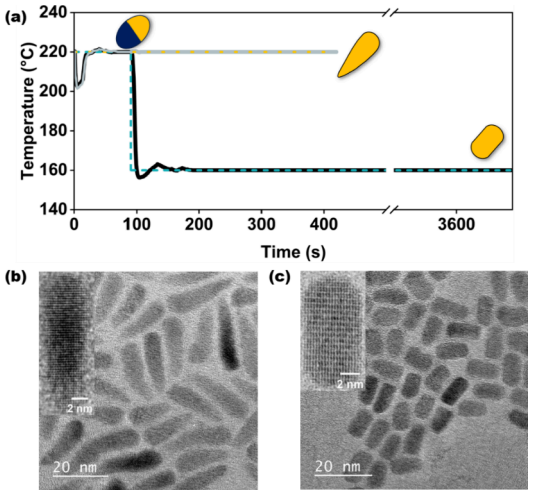

Figure 7. (a) Temperature profile of two different types of $CuGaS_2$ nanorod synthesis. Dashed and dotted lines are the input temperature profiles. Solid lines are the measured temperature profiles for tapering (gray) and nontapering (black) nanorods. The initial fast decrease and recovery in temperature at the beginning of the reaction for both cases correspond to $Cu_{2-x}S$ seed injection. Schematics of the intermediate Janus particle and final $CuGaS_2$ nanorods are shown in the inset. (b) TEM image of tapering $CuGaS_2$ nanorods $CuGaS_2$ obtained from keeping the temperature at 220 °C for the entire reaction, corresponding to the gray line temperature profile in (a). HRTEM image of a single tapering nanorod is shown in the inset. (c) TEM image of $CuGaS_2$ nanorods without tapering obtained from reaction corresponding to the black line temperature profile in (a). HRTEM image of a single nontapering nanorod is shown in the inset.

220 °C, but the second reaction included a temperature quench from 220 to 160 °C prior to reaching t^*. Figure 7a shows the temperature profiles measured during the two reactions. Figure 7b and Figure 7c show the TEM images of the final product for the constant temperature and temperature quench cases, respectively. In the constant temperature case (Figure 7b), the usual tapering of $CuGaS_2$ nanorods is observed. On the other hand, the tapering is essentially eliminated for the temperature quench case (Figure 7c). These results show how two morphologies can be intended and achieved, demonstrating the importance and usefulness of quantifying reaction kinetics.

CONCLUSIONS

We have shown how near-spherical $Cu_{2-x}S$ NCs evolve into $CuGaS_2$ nanorods of different lengths and degree of tapering at different reaction temperatures. The seed $Cu_{2-x}S$ NCs undergo an early-stage Cu loss, and the length and the tapering of the resulting $CuGaS_2$ nanorods are strongly dependent on temperature. Through a simple kinetic model, we have been able to quantify the epitaxial growth and cation exchange that are occurring concurrently. Epitaxial growth of $Cu_{2-x}S$ seeds has an activation energy of 96 kJ mol^{-1}, whereas cation exchange has a higher activation energy of 202 kJ mol^{-1}. The latter requires a heterogeneous nucleation process before two-dimensional growth can proceed. At the beginning of the reaction, epitaxial growth of the seed NCs prevails with a delayed onset for cation exchange. Cation exchange becomes

https://doi.org/10.1021/jacs.4c17582
J. Am. Chem. Soc. 2025, 147, 9566−9575

dominant soon after. Tapering then begins when the cation exchange rate becomes faster than the epitaxy rate, causing the $Cu_{2-x}S$ phase to decrease in volume. By rapidly cooling to 160 °C before the cation exchange rate overtakes the epitaxial rate, tapering can be effectively eliminated. These results provide a path to precise tailoring of morphologies and compositions of NCs, from $Cu_{2-x}S/CuGaS_2$ heterostructured particles with different Cu and Ga ratios to $CuGaS_2$ nanorods of variable length and degree of tapering, through easily accessible reaction parameters of temperature and time.

EXPERIMENTAL SECTION

Materials. Copper(II) sulfate pentahydrate ($CuSO_4{\cdot}5H_2O$, ≥98%), gallium(III) acetylacetonate ($Ga(acac)_3$, 99.99%), oleic acid (OA, 90% technical grade), 1-DDT (≥98%), ethanol, methanol, toluene, 1-butanol, and chloroform were purchased from Sigma-Aldrich. All chemicals were used as received.

Synthesis of 7 nm $Cu_{2-x}S$ NCs. $Cu_{2-x}S$ NCs were prepared according to a method previously reported in the literature[26] with some modifications. 0.624 g of $CuSO_4{\cdot}5H_2O$ (2.5 mmol), 18 mL of OA, and 24 mL of 1-DDT were placed into a 100 mL three-neck round-bottomed flask. The solution was degassed under vacuum while being stirred at room temperature for half an hour. The solution was then heated to 250 °C at a rate of about 30 °C/min under an argon atmosphere. The temperature was set to 200 °C after it reached 250 °C, where it was held for 25 min. Once the synthesis was complete, the mixture was rapidly cooled to 110 °C via an air jet and then quenched with 15 mL of toluene. Methanol and butanol (around 1:1) were added to the flask, and the product was isolated by centrifugation at 2500 rpm for 15 min. After decanting the supernatant, the product remaining in the tube was redispersed in 20 mL of toluene and kept in a glovebox until used for further reactions.

$CuGaS_2$ Nanorod Synthesis. $CuGaS_2$ nanorods were synthesized first by taking 2 mL of the previously synthesized $Cu_{2-x}S$ NCs in toluene, cleaning them by adding ethanol and chloroform, and centrifuging. After repeating three times and decanting the supernatant, the NCs were redispersed in 1 mL of 1-DDT. In a separate reaction flask, 0.0918 g (0.25 mmol) of $Ga(acac)_3$ was combined with 5 mL of 1-DDT. The molar ratio of Ga added to Cu used in the initial $Cu_{2-x}S$ NC synthesis was 1:1. The mixture was degassed while being stirred for a short period before being heated to the desired reaction temperature (from 160 to 240 °C). When the solution reached the desired temperature, the cleaned $Cu_{2-x}S$ seeds were swiftly injected into the mixture. Aliquots were acquired throughout the reaction. These aliquots were cleaned by adding toluene and acetone and centrifuging for three times before further characterization.

Characterization. Vis-NIR absorption measurements were taken in a 1.7 mL, 0.5 cm-path-length cuvette on a Cary 5G UV−vis-NIR spectrometer, and chloroform was used as solvent. TEM samples were prepared by drop-casting a dispersion of particles diluted by toluene on an ultrathin 200 carbon square mesh, gold grid. The grids were annealed at 80 °C for 24 h and plasma cleaned before being loaded into the microscope. HRTEM images were taken on a 200 kV JEOL 2100FS Cryo-TEM. STEM-HAADF and EDX were taken on a 200 kV FEI Talos operating at 20 kV energy dispersion using the Cu K-line, Ga K-line, and S K-line. Samples for X-ray diffraction analysis were prepared by drop-drying NC solution on a silicon wafer and annealing at 80 °C for 24 h under the vacuum. XRD measurements were performed with a Bruker D8 Advance XRD/XRR System. The volumes of particles were measured by analyzing HRTEM images of the aliquots acquired during the reaction. A stereological method was used to estimate the 3D volume of respective species using 2D images.[43] The procedure is described in detail in the Supporting Information.

ASSOCIATED CONTENT

Supporting Information

The Supporting Information is available free of charge at https://pubs.acs.org/doi/10.1021/jacs.4c17582.

HRTEM, STEM, and EDX results; details and example of volume estimation; photographs of control experiments; plots of fitting parameters c_0, g_0, and n versus temperature; and evaluation of the Avrami exponent (PDF)

AUTHOR INFORMATION

Corresponding Author

Moonsub Shim − *Department of Materials Science and Engineering and Seitz Materials Research Laboratory, University of Illinois at Urbana−Champaign, Urbana, Illinois 61801, United States;* orcid.org/0000-0001-7781-1029; Email: mshim@illinois.edu

Author

Yunpei Duan − *Department of Materials Science and Engineering and Seitz Materials Research Laboratory, University of Illinois at Urbana−Champaign, Urbana, Illinois 61801, United States;* orcid.org/0009-0000-1169-2311

Complete contact information is available at: https://pubs.acs.org/10.1021/jacs.4c17582

Notes

The authors declare no competing financial interest.

ACKNOWLEDGMENTS

Financial support from the U.S. National Science Foundation (Grant No. 2403367) is gratefully acknowledged. Experiments were carried out in part in the Frederick Seitz Materials Research Laboratory Central Research Facilities, University of Illinois.

REFERENCES

(1) McDaniel, H.; Fuke, N.; Pietryga, J. M.; Klimov, V. I. Engineered CuInSe x S2−x quantum dots for sensitized solar cells. *J. Phys. Chem. Lett.* **2013**, *4* (3), 355−361.

(2) Lim, L. J.; Zhao, X.; Tan, Z. Non-Toxic CuInS2/ZnS Colloidal Quantum Dots for Near-Infrared Light-Emitting Diodes. *Adv. Mater.* **2023**, *35* (28), 2301887.

(3) Poulose, A. C.; Veeranarayanan, S.; Aravind, A.; Nagaoka, Y.; Yoshida, Y.; Maekawa, T.; Kumar, D. S. Synthesis of CuAlS2 nanocrystals and their application in bio-imaging. *Mater. Express* **2012**, *2* (2), 94−104.

(4) Li, L.; Pandey, A.; Werder, D. J.; Khanal, B. P.; Pietryga, J. M.; Klimov, V. I. Efficient synthesis of highly luminescent copper indium sulfide-based core/shell nanocrystals with surprisingly long-lived emission. *J. Am. Chem. Soc.* **2011**, *133* (5), 1176−1179.

(5) Hase, S.; Iso, Y.; Isobe, T. Bandgap-tuned fluorescent CuGaS 2/ZnS core/shell quantum dots for photovoltaic applications. *J. Mater. Chem. C* **2022**, *10* (9), 3523−3530.

(6) Du, C.-F.; You, T.; Jiang, L.; Yang, S.-Q.; Zou, K.; Han, K.-L.; Deng, W.-Q. Controllable synthesis of ultrasmall CuInSe 2 quantum dots for photovoltaic application. *Rsc Adv.* **2014**, *4* (64), 33855−33860.

(7) Zhou, N.; Zhao, H.; Li, X.; Li, P.; You, Y.; Cai, M.; Xia, L.; Zhi, H.; Channa, A. I.; Wang, Z. M.; Tong, X. Activating Earth-abundant element-based colloidal copper chalcogenide quantum dots for photodetector and optoelectronic synapse applications. *ACS Mater. Lett.* **2023**, *5* (4), 1209−1218.

(8) Tomić, S.; Bernasconi, L.; Searle, B. G.; Harrison, N. M. Electronic and optical structure of wurtzite CuInS2. *J. Mater. Chem. C* **2014**, *118* (26), 14478−14484.
(9) Levcenko, S.; Syrbu, N.; Tezlevan, V.; Arushanov, E.; Doka-Yamigno, S.; Schedel-Niedrig, T.; Lux-Steiner, M. C. Optical spectra and energy band structure of single crystalline CuGaS2 and CuInS2. *J. Phys. Condens. Matter Phys.* **2007**, *19* (45), No. 456222.
(10) Reiss, P.; Carriere, M.; Lincheneau, C.; Vaure, L.; Tamang, S. Synthesis of semiconductor nanocrystals, focusing on nontoxic and earth-abundant materials. *Chem. Rev.* **2016**, *116* (18), 10731−10819.
(11) Kim, Y.-K.; Ahn, S.-H.; Chung, K.; Cho, Y.-S.; Choi, C.-J. The photoluminescence of CuInS 2 nanocrystals: effect of non-stoichiometry and surface modification. *J. Mater. Chem.* **2012**, *22* (4), 1516−1520.
(12) Chen, B.; Zhong, H.; Zhang, W.; Tan, Z. a.; Li, Y.; Yu, C.; Zhai, T.; Bando, Y.; Yang, S.; Zou, B. Highly emissive and color-tunable CuInS2-based colloidal semiconductor nanocrystals: off-stoichiometry effects and improved electroluminescence performance. *Adv. Funct. Mater.* **2012**, *22* (10), 2081−2088.
(13) Chen, B.; Zheng, W.; Chun, F.; Xu, X.; Zhao, Q.; Wang, F. Synthesis and hybridization of $CuInS_2$ nanocrystals for emerging applications. *Chem. Soc. Rev.* **2023**, *52* (23), 8374−8409.
(14) Drake, G. A.; Keating, L. P.; Shim, M. Design principles of colloidal nanorod heterostructures. *Chem. Rev.* **2023**, *123* (7), 3761−3789.
(15) Akdas, T.; Walter, J.; Segets, D.; Distaso, M.; Winter, B.; Birajdar, B.; Spiecker, E.; Peukert, W. Investigation of the size−property relationship in CuInS 2 quantum dots. *Nanoscale* **2015**, *7* (43), 18105−18118.
(16) Akdas, T.; Haderlein, M.; Walter, J.; Apeleo Zubiri, B.; Spiecker, E.; Peukert, W. Continuous synthesis of CuInS 2 quantum dots. *RSC Adv.* **2017**, *7* (17), 10057−10063.
(17) Park, J.; Kim, S.-W. CuInS 2/ZnS core/shell quantum dots by cation exchange and their blue-shifted photoluminescence. *J. Mater. Chem.* **2011**, *21* (11), 3745−3750.
(18) Hinterding, S. O.; Berends, A. C.; Kurttepeli, M.; Moret, M.-E.; Meeldijk, J. D.; Bals, S.; Van Der Stam, W.; de Mello Donega, C. Tailoring Cu+ for Ga3+ Cation Exchange in Cu2−x S and CuInS2 Nanocrystals by Controlling the Ga Precursor Chemistry. *ACS Nano* **2019**, *13* (11), 12880−12893.
(19) Akkerman, Q. A.; Genovese, A.; George, C.; Prato, M.; Moreels, I.; Casu, A.; Marras, S.; Curcio, A.; Scarpellini, A.; Pellegrino, T.; Manna, L.; Lesnyak, V. From binary Cu2S to ternary Cu−In−S and quaternary Cu−In−Zn−S nanocrystals with tunable composition via partial cation exchange. *ACS Nano* **2015**, *9* (1), 521−531.
(20) Xia, C.; Van Oversteeg, C. H.; Bogaards, V. C.; Spanjersberg, T. H.; Visser, N. L.; Berends, A. C.; Meeldijk, J. D.; De Jongh, P. E.; de Mello Donega, C. Synthesis and Formation Mechanism of Colloidal Janus-Type Cu2−x S/CuInS2 Heteronanorods via Seeded Injection. *ACS Nano* **2021**, *15* (6), 9987−9999.
(21) Ashfaq, A.; Tahir, S.; Rehman, U. u.; Ali, A.; Ashfaq, H. F.; Ahmad, W.; Mushtaq, S.; Saeed, R.; Haneef, M.; Khan, K. M.; Shabbir, K. Structural, morphological and thermoelectric properties of copper deficient and excessive Cu2-xS nanoparticles with (x= 0−0.3). *Surf. Interfaces* **2022**, *30*, No. 101965.
(22) Fenton, J. L.; Steimle, B. C.; Schaak, R. E. Structure-selective synthesis of wurtzite and zincblende ZnS, CdS, and CuInS2 using nanoparticle cation exchange reactions. *Inorg. Chem.* **2019**, *58* (1), 672−678.
(23) Steimle, B. C.; Fagan, A. M.; Butterfield, A. G.; Lord, R. W.; McCormick, C. R.; Di Domizio, G. A.; Schaak, R. E. Experimental insights into partial cation exchange reactions for synthesizing heterostructured metal sulfide nanocrystals. *Chem. Mater.* **2020**, *32* (13), 5461−5482.
(24) Steimle, B. C.; Fenton, J. L.; Schaak, R. E. Rational construction of a scalable heterostructured nanorod megalibrary. *Science* **2020**, *367* (6476), 418−424.
(25) Lee, S.; Baek, S.; Park, J. P.; Park, J. H.; Hwang, D. Y.; Kwak, S. K.; Kim, S.-W. Transformation from Cu2−x S Nanodisks to Cu2−x S@ CuInS2 Heteronanodisks via Cation Exchange. *Chem. Mater.* **2016**, *28* (10), 3337−3344.
(26) Van Der Stam, W.; Berends, A. C.; Rabouw, F. T.; Willhammar, T.; Ke, X.; Meeldijk, J. D.; Bals, S.; de Mello Donega, C. Luminescent CuInS2 Quantum Dots by Partial Cation Exchange in Cu2−x S Nanocrystals. *Chem. Mater.* **2015**, *27* (2), 621−628.
(27) Zhai, Y.; Flanagan, J. C.; Shim, M. Lattice Strain and Ligand Effects on the Formation of Cu2−x S/I-III-VI2 Nanorod Heterostructures through Partial Cation Exchange. *Chem. Mater.* **2017**, *29* (14), 6161−6167.
(28) Thiel, F.; Palencia, C.; Weller, H. Kinetic Analysis of the Cation Exchange in Nanorods from Cu2−x S to CuInS2: Influence of Djurleite's Phase Transition Temperature on the Mechanism. *ACS Nano* **2023**, *17* (4), 3676−3685.
(29) Ho, T.-L. Hard soft acids bases (HSAB) principle and organic chemistry. *Chem. Rev.* **1975**, *75* (1), 1−20.
(30) Miszta, K.; Gariano, G.; Brescia, R.; Marras, S.; De Donato, F.; Ghosh, S.; De Trizio, L.; Manna, L. Selective cation exchange in the core region of Cu2−x Se/Cu2−x S core/shell nanocrystals. *J. Am. Chem. Soc.* **2015**, *137* (38), 12195−12198.
(31) Le, H. K.; Xiong, H.; Page, B. A.; Garcia-Herrera, L. F.; McAllister, H. P.; Li, B. C.; Wang, H.; Plass, K. E. Effects of I2 on Cu2−x S Nanoparticles: Enabling Cation Exchange but Complicating Plasmonics. *ACS mater. lett.* **2020**, *2* (2), 140−146.
(32) Keating, L.; Shim, M. Mechanism of morphology variations in colloidal CuGaS 2 nanorods. *Nanoscale Adv.* **2021**, *3* (18), 5322−5331.
(33) Wark, S. E.; Hsia, C.-H.; Son, D. H. Effects of ion solvation and volume change of reaction on the equilibrium and morphology in cation-exchange reaction of nanocrystals. *J. Am. Chem. Soc.* **2008**, *130* (29), 9550−9555.
(34) Mu, L.; Wang, F.; Sadtler, B.; Loomis, R. A.; Buhro, W. E. Influence of the nanoscale kirkendall effect on the morphology of copper indium disulfide nanoplatelets synthesized by ion exchange. *ACS Nano* **2015**, *9* (7), 7419−7428.
(35) Oh, N.; Keating, L. P.; Drake, G. A.; Shim, M. CuGaS2−CuInE2 (E= S, Se) colloidal nanorod heterostructures. *Chem. Mater.* **2019**, *31* (6), 1973−1980.
(36) Li, Q.; Zou, C.; Zhai, L.; Shen, J.; Zhang, L.; Yu, H.; Yang, Y.; Chen, X. a.; Huang, S. Growth of wurtzite CuGaS2 nanoribbons and their photoelectrical properties. *J. Alloys Compd.* **2013**, *567*, 127−133.
(37) Adhikari, S. D.; Dutta, A.; Prusty, G.; Sahu, P.; Pradhan, N. Symmetry break and seeded 2D anisotropic growth in ternary CuGaS2 nanocrystals. *Chem. Mater.* **2017**, *29* (12), 5384−5393.
(38) Luther, J. M.; Jain, P. K.; Ewers, T.; Alivisatos, A. P. Localized surface plasmon resonances arising from free carriers in doped quantum dots. *Nat. Mater.* **2011**, *10* (5), 361−366.
(39) Xiao, N.; Zhu, L.; Wang, K.; Dai, Q.; Wang, Y.; Li, S.; Sui, Y.; Ma, Y.; Liu, J.; Liu, B.; Zou, G.; Zou, B. Synthesis and high-pressure transformation of metastable wurtzite-structured CuGaS 2 nanocrystals. *Nanoscale* **2012**, *4* (23), 7443−7447.
(40) Zhang, D.; Wong, A. B.; Yu, Y.; Brittman, S.; Sun, J.; Fu, A.; Beberwyck, B.; Alivisatos, A. P.; Yang, P. Phase-selective cation-exchange chemistry in sulfide nanowire systems. *J. Am. Chem. Soc.* **2014**, *136* (50), 17430−17433.
(41) Pearson, R. G. Absolute electronegativity and hardness: application to inorganic chemistry. *Inorg. Chem.* **1988**, *27*, 734−740.
(42) Rudzinski, W.; Plazinski, W. Studies of the kinetics of solute adsorption at solid/solution interfaces: on the possibility of distinguishing between the diffusional and the surface reaction kinetic models by studying the pseudo-first-order kinetics. *J. Phys. Chem. C* **2007**, *111* (41), 15100−15110.
(43) Jensen, E. V.; Gundersen, H. J. G. The rotator. *J. Microsc.* **1993**, *170* (1), 35−44.
(44) Blázquez, J. S.; Romero, F. J.; Conde, C. F.; Conde, A. A review of different models derived from classical Kolmogorov, Johnson and Mehl, and Avrami (KJMA) theory to recover physical meaning in solid-state transformations. *Phys. Status Solidi B* **2022**, *259* (6), 2100524.

https://doi.org/10.1021/jacs.4c17582
J. Am. Chem. Soc. 2025, 147, 9566−9575

(45) Avrami, M. Granulation, phase change, and microstructure kinetics of phase change III. *J. Chem. Phys.* **1941**, *9* (2), 177−184.
(46) De Trizio, L.; Manna, L. Forging colloidal nanostructures via cation exchange reactions. *Chem. Rev.* **2016**, *116* (18), 10852−10887.

https://doi.org/10.1021/jacs.4c17582
J. Am. Chem. Soc. 2025, 147, 9566−9575